

Chapter 5

The UT-CERN Cos-theta LHC-Type Nb₃Sn Dipole Magnet



Herman H. J. ten Kate, Andries den Ouden, and Daniel Schoerling

Abstract This chapter reports on the University of Twente (UT)–European Organization for Nuclear Research (CERN) cos-theta LHC-type Nb₃Sn dipole magnet program. In this program an experimental 1 m long two-layer cos-theta dipole magnet was developed using Rutherford cables made with powder-in-tube Nb₃Sn composite wires. The magnet reached a magnetic field of 11.3 T in a bore of 50 mm.

5.1 Introduction

To continue the successful development of Nb₃Sn dipoles started with the CERN–ELIN collaboration (see Chap. 4), the Applied Superconductivity Centre at the University of Twente, the Netherlands, initiated a collaboration with the National Institute for Subatomic Physics (Nikhef), the Energy Research Centre of the Netherlands (ECN), the European Organization for Nuclear Research (CERN), and the companies HOLEC and SMIT WIRE. The aim of the collaboration was to design and build an experimental 1 m long Large Hadron Collider (LHC)-type dipole magnet to convincingly break through the 10 T barrier experienced so far. In this program specific novel ideas and high current density powder-in-tube (PIT) Nb₃Sn composite wires were envisaged.

The main funding for this project was granted by the Netherlands Technology Foundation STW, with some contributions by companies, and was supported by

H. H. J. ten Kate (✉)
University of Twente, Enschede, Netherlands

CERN (European Organization for Nuclear Research), Meyrin, Genève, Switzerland
e-mail: Herman.TenKate@cern.ch

A. den Ouden
Radboud University, Nijmegen, Netherlands
e-mail: a.denouden@science.ru.nl

D. Schoerling
CERN (European Organization for Nuclear Research), Meyrin, Genève, Switzerland
e-mail: Daniel.Schoerling@cern.ch

CERN through the magnet test effort. The magnet parameters were chosen such to meet the LHC requirements at that time, i.e., a two-layer design with a minimum magnetic field of 10 T at 4.4 K within a free aperture of 50 mm (ten Kate et al. 1991).

Back then, the race between Nb-Ti dipole magnets operating at 1.9 K and Nb₃Sn magnets operating at 4.4 K was decided in favor of Nb-Ti technology. Nb₃Sn conductor technology was considered not sufficiently mature to be used reliably and efficiently for large-scale production. Moreover, the cost of Nb₃Sn conductor and magnet production in combination with the lack of experience with large-scale high current density Nb₃Sn superconductor and coil manufacturing in industry added to the decision to use Nb-Ti dipole magnet technology operating at 1.9 K for the LHC. Operation at 1.9 K was considered feasible following the progress demonstrated in cryogenic technology (Claudet and Aymar 1990).

In 1989, however, it was also clear that for a large number of Nb-Ti magnets connected in series it would hardly be possible to attain reliable 10 T operation, and indeed the operating magnetic field of the LHC was later reduced to 8.33 T. This limitation retained interest in further research towards Nb₃Sn LHC-type dipole magnets.

In the Nb₃Sn dipole magnet landscape of 1987, the program known as the Model Single of the University of Twente (MSUT), showed very few magnets with a real bore, and all performed well below 10 T. The latest was the CERN-ELIN magnet, which achieved only 9.7 T due to the limited current density in the bronze route Nb₃Sn wires used. In order to break through the 10 T barrier, a new project was launched with the ambition:

1. To exploit the potential of the Powder-in-Tube (PIT) Nb₃Sn conductor by targeting a magnetic field well above 10 T at 4.4 K (the LHC target in 1988);
2. To meet the LHC dipole parameters;
3. To perform research on PIT wires and cables for increasing the wire engineering critical current density $J_c(B, T)$, reduction of filament size, thereby reducing magnetization effects, and the degradation of I_c as a function of strain; and
4. To develop a dedicated design and technology to realize a 1 m long model single-aperture dipole magnet following a few new ideas to overcome problems with traditional designs.

As the requirements for Nb₃Sn conductor are fundamentally different from those for Nb-Ti conductor, the design has been re-worked from scratch and dedicated solutions addressing the specific challenges of using Nb₃Sn conductor and the wind-and-react (W&R) route were developed. In addition, based on a review of the manufacturing and performance problems of earlier Nb₃Sn dipole magnets, in particular concerning degradation and training, it has been decided to try out new solutions for achieving a better performance. Major investigations in the frame of this program included the development of the following:

1. A two-layer graded coil using 22 and 17 mm wide Rutherford cables with 1.26 and 0.98 mm strand diameters for the inner and outer layers, respectively. A two-layer design was chosen for two reasons: firstly to limit the coil winding cost,

and secondly to demonstrate the beneficial effect of stiff cables on the coil's training behavior.

2. New cable insulation based on a folded glass-mica tape wrapped with glass-fiber ribbon. The idea of using a dielectric mica film was motivated by reducing the risk of electrical shorts in the coil windings, in particular in full-size long magnets, and by reducing the risk of micro-cracking in windings.
3. A continuous support of the conductors at the transition from the straight part into the coil ends using strip-like end spacers brazed to the longitudinal wedges. Usually in magnets, spacers are not connected to the wedges, and a discontinuity or locally softer cable support is present, which may cause training quenches in magnets. Indeed, in this type of dipole magnet many training quenches have their origin in this area. Therefore it was considered necessary to avoid such a discontinuity.
4. A natural bending of the conductor over the coil heads to achieve a minimum stress layout even before cable heat treatment. The disadvantage of this method is that the cross-section of the coil head looks irregular since the cables are not forced to follow the shape of the predetermined end spacers.
5. A coil heat treatment without any constraint in the end spacer area. During heat treatment and roughly 3% Nb₃Sn volume expansion, the conductor can freely move and settle.
6. After the heat treatment, all local voids in the coil heads were securely filled with glass fibers. This filling was considered important to avoid any substantial voids filled with pure resin that may cause micro-cracks and, thus, training quenches.
7. A layer-to-layer joint using a superconducting shunt. In this way a layer jump can be avoided leading to a more uniform mechanical winding pack. The superconducting shunt was inserted and soldered after coil heat treatment but before resin vacuum impregnation.
8. Vacuum impregnation of the coil windings with Ciba-Geigy, Switzerland resin system composed of Araldite MY740 epoxy, HY906 hardener, and DY062 accelerator.
9. Closed, shrink-fit aluminum-alloy ring-collars for achieving optimal coil support without overstressing the Nb₃Sn. This type of collar and material were chosen to eliminate the risk of conductor degradation when using split collars and keys, and avoiding the risk of using a collaring press.

The PIT Nb₃Sn wire was developed and manufactured by ECN while cabling was performed at the Lawrence Berkeley National Laboratory (LBNL) in Berkeley, USA. After wire production, ECN closed its Nb₃Sn wire facilities. All wire-making equipment and knowledge were transferred, first to the University of Twente for a few years, and later in 1991 to the university spin-off company Shape Metal Innovation (SMI) in Enschede, The Netherlands. SMI further developed PIT conductors for many years while supported by Twente University, and delivered PIT Nb₃Sn wires for use in high-field magnets, in particular in various dipole magnets at the Fermi National Accelerator Laboratory and CERN. Finally, in 2006 the PIT technology was acquired from SMI by Bruker-EAS.

The 1 m, single-aperture dipole model magnet was manufactured in a five-year project from 1990 to 1995 at the University of Twente and tested first in 1995 and again in 1997 at CERN. The details of magnet design, technology development, system manufacturing, and magnet performance are discussed below.

5.2 Magnet Design

5.2.1 *Electromagnetic Design*

The initial twin-aperture electromagnetic design was optimized according to the following criteria (ter Avest et al. 1991):

- To minimize the amount of conductor, a shell-type (also known as cos-theta) design was chosen with graded current density, implying a higher current density in the outer layer than in the inner layer by reducing the cable cross-section.
- To ease operation, the same operating current (≤ 20 kA) and similar load-line margins were foreseen.
- In view of the large scale of production, maintaining simplicity (considered to be important), costs, and labor, the number of layers was kept to two.
- To reach a field quality on the level of 10^{-4} , the design and fabrication tolerances needed to be small.
- To produce a stable cable, the number of strands per cable and the diameter of the strands needed to remain within a practical range.

These constraints are partly contradictory, and for practical reasons the following criteria were used: a cable thickness < 3 mm, a maximum angle of the layers $\leq 70^\circ$, and ≤ 36 strands per cable.

For a field of 10 T the overall current density was assumed to be 453 A/mm^2 and the non-Cu current density 1373 A/mm^2 . These numbers include 13% overall void fraction in the cable, 16% area for the insulation thickness, and 10% operational margin on the load line for both layers.

The first round of optimization focused on a 2D optimization of a single-aperture magnet, assuming an iron yoke with a round inner diameter of 200 mm, infinite outer diameter and permeability, and the same cable properties for all layers. Figure 5.1 shows the simplified model used for the first optimization.

The field distribution in such a configuration can be calculated with analytical equations (Perin 1973; ter Avest et al. 1991). After setting the magnetic field to 11.5 T and the current density in the inner layer, the geometry was optimized by eliminating the two multipoles b_3 and b_5 . This optimization was fast and produced two classes of solutions: one with maximum angles of about $70^\circ/45^\circ$ (inner/outer layer) and one with maximum angles of about $50^\circ/80^\circ$. The last design option, however, requires more superconductor, and a difficult mechanical support structure, and was, therefore, abandoned.

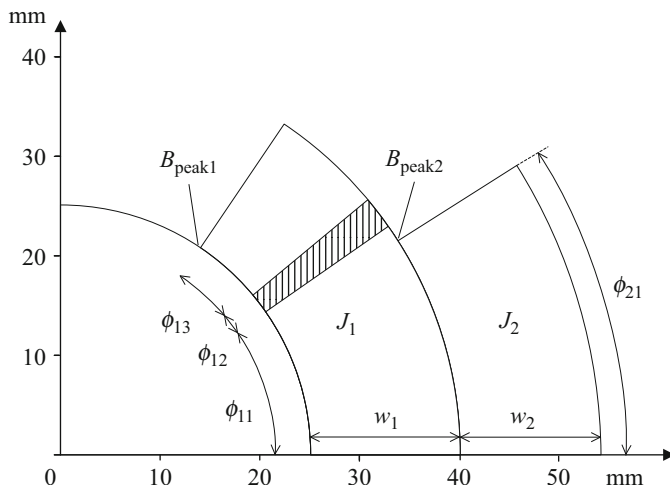


Fig. 5.1 The two-layer coil cross-section: B_{peak} – peak field in a layer, w – width of a layer, J – overall current density, and ϕ angle of a circular segment. The unit on both axes is mm. (Modified from ter Avest et al. 1991)

As the next step, the grading ratio between the inner and outer layers was optimized under the assumption that the transport current and the number of strands in the outer layer are fixed. It can be shown that, for an increasing ratio of w_2/w_1 , the maximum angle of the coil increases. The total amount of superconductor is almost invariant to a w_2/w_1 variation for $w_2/w_1 \geq 0.8$. Therefore, a grading ratio of $w_2/w_1 = 0.8$ ($J_2/J_1 = 1.6$) was selected in order to minimize the top angle of the inner layer. Then, the higher multipoles b_7 and b_9 were minimized. Since more degrees of freedom were required, two additional wedges were added.

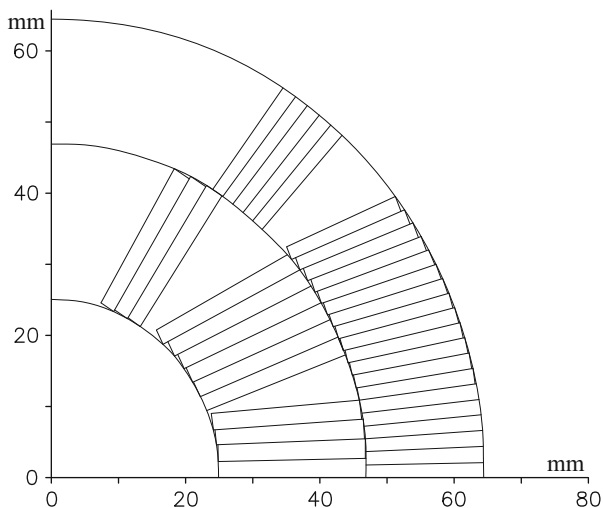
In the final step, the round shell segments were converted into keystoneed cable segments and were optimized around the previously determined point. The geometric design multipoles (expressed relative to B_1) are $(b_3, b_5, b_7, b_9) = (-0.06, -0.5, -0.6, 0.3) \cdot 10^{-4}$. With a maximum angle $\phi_1 = 70.5^\circ$ and $\phi_2 = 58.4^\circ$, the required operating current is 17.7 kA. The cable parameters are presented in Table 5.1. The coil cross-section is shown in Fig. 5.2. A detailed treatment of the electromagnetic design optimization is given in ter Avest et al. (1991).

5.2.2 Conductor Choice and Parameters

To limit the coil width by two typical maximum widths of the Rutherford cable and enabling a twin-aperture design with an inter-beam spacing of 194 mm, the coil width was limited to around 35 mm. This limitation imposed for the reference design field level of 10 T a critical current density J_c of about 1580 A/mm² at 10 T in the non-copper part of the conductor, assuming a Cu/non-Cu ratio of 1.

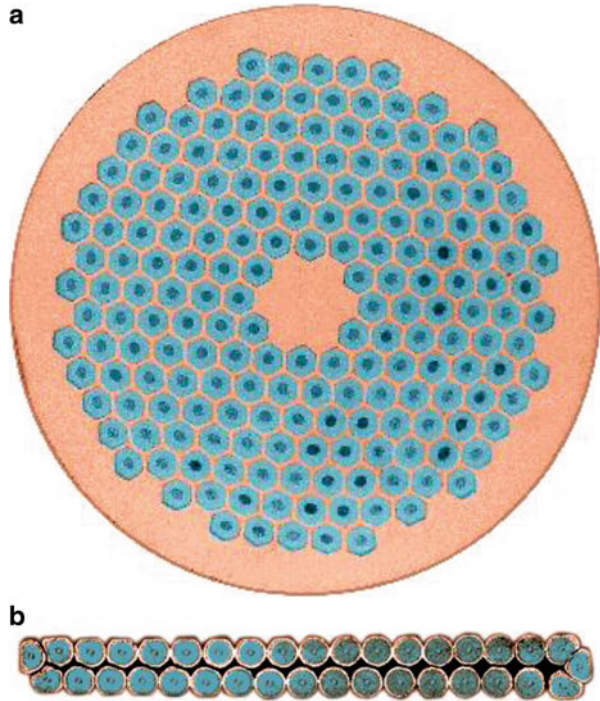
Table 5.1 Nb₃Sn Rutherford cables and strand parameters for the inner and outer layers of the coils in twin-aperture configuration for the 10 and 11.5 T versions

Parameter	10 T design		11.5 T design	
	Inner layer	Outer layer	Inner layer	Outer layer
Thin edge (mm)	2.19	1.47	1.98	1.54
Thick edge (mm)	2.69	1.79	2.47	1.93
Bare cable width (mm)	16.8	16.8	21.7	17.4
Strand diameter (mm)	1.35	0.98	1.26	1.00
Cu fraction (%)	50	50	56	56
Filament diameter (μm)	–	–	42	32
Number of filaments	–	–	192	192
Filament twist pitch (mm)	–	–	30	30
Number of strands	24	36	33	33
RRR value	≥100	≥100	≥100	≥100
Cable pitch (mm)	≥120	≥120	150	150
Cable unit length (m)	4 × 25	4 × 40	4 × 25	4 × 40
Insulation thickness (mm)	0.14	0.14	0.14	0.14
Nominal current (kA)	16.0		17.7	
B_{peak} at I_{nom} (T)	10.2	8.7	11.9	9.6

Fig. 5.2 Optimized cross-section of the 11.5 T design coil. The unit on both axes is mm. (Modified from ter Avest et al. 1991)

This high current density had to be achieved with small filaments in order to minimize magnetization effects, to improve field quality, and to minimize heat loss. First estimates called for an effective filament diameter below 10 μm. The combination of high critical current density and sufficiently small filaments was not available at the time. In the MSUT project, the focus was laid, therefore, on the conductor with the best performance available: the ECN PIT multi-filamentary wire. The non-copper critical current density J_c measured on short samples for these wires

Fig. 5.3 (a) Cross-section of a 192-filament PIT Nb₃Sn wire with a pure copper fraction of 55%; and (b) a Rutherford cable made from this wire featuring 36 strands of 0.90 mm diameter, cable size = 1.45/1.77 × 16.70 mm. (Modified from ten Kate et al. 1991)

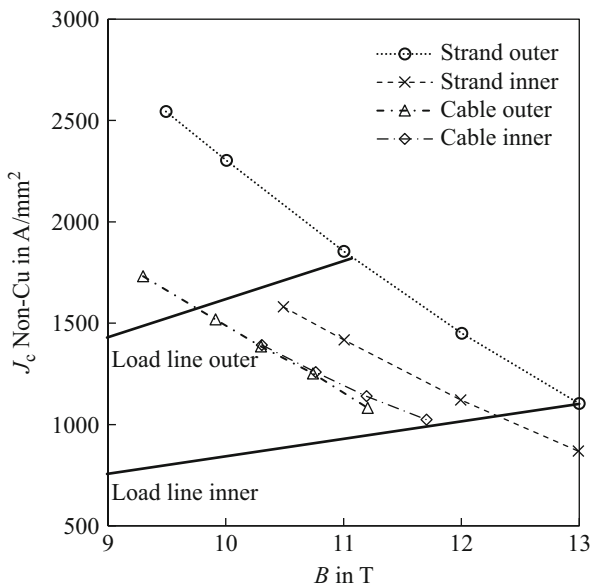


was about 2000 A/mm² at 10 T and 4.2 K, about a factor of 2.5 higher than in bronze conductors: at the expense, however, of a larger filament size. The program subsequently focused on decreasing the filament diameter, maintaining the same critical current density, increasing the unit lengths, and producing Rutherford cables with limited critical current degradation.

In an effort to reduce the filament size below $D_{\text{eff}} \leq 20 \mu\text{m}$ a double-stacking method was developed at ECN. Billets with 18, 19, and 37 spokes were stacked into billets with $18 \times 18 = 324$ ($D_{\text{eff}} = 29 \mu\text{m}$), $36 \times 19 = 684$ ($D_{\text{eff}} = 21 \mu\text{m}$), and $36 \times 37 = 1332$ ($D_{\text{eff}} = 15 \mu\text{m}$) sub-elements. After assembly, they were drawn into wires with a diameter of 0.85 mm, and short sample measurements were performed (Hornsveld et al. 1988), confirming critical current densities of about 1900 A/mm² at 10 T and 4.2 K. The process, however, appeared rather costly, took a long time, and it was impossible to reliably draw sufficiently long lengths without breakage. Therefore, the single-stack wire design with 192 filaments was taken as a baseline and was used to produce about 75 km of wire, weighing about 500 kg, making up sufficient unit lengths. Tests of keystone cables (Fig. 5.3) were performed at ECN and later at LBNL. Critical current measurements revealed little degradation, rendering a critical current of 30 kA at 8.7 T.

Based on this success, the magnet design was reiterated and the target magnetic field was increased from 10 T to 11.5 T for a twin-aperture design and 11.0 T for a single-aperture design, using a slightly larger cable. The cable parameters for the two

Fig. 5.4 Measured non-Cu J_c vs. magnetic field before (strand) and after cabling (cable) for inner and outer layer cables, averaged over at least five samples per case. The load lines for the inner and outer layers are also shown. (Modified from den Ouden et al. 1994)



design proposals for a bore field of 10 T (abandoned) and 11.5 T (pursued) are summarized in Table 5.1. At that time the cables for the 11.5 T design were the largest Rutherford cables ever made for use in an accelerator dipole magnet.

After the study of various designs, it was decided to construct a single-aperture dipole configuration. Due to a smaller yoke and the absence of magnetic field enhancement by a second aperture, the field factor of the model magnet was strongly affected. Where the twin-aperture system could generate 11.5 T at 17.7 kA, the single-aperture magnet would reach only 11.0 T at about 18.7 kA. This still impressive target field, however, appeared well reachable with the conductor properties. Figure 5.4 shows the results of critical current measurements on wire and cable samples together with the load lines for inner and outer conductor layers. In both cases, an I_c criterion of 5 $\mu\text{V/m}$ was used. The strands produced by ECN for the final coils were their last production before their facilities were closed. This impeded stable production control and rejection of less-well performing batches if required. The data presented in Fig. 5.4 therefore represent an average of different batches with an unusual large scatter in critical current values of typically 10%.

Despite the abovementioned scatter between different batches of a single type of strand, the degradation due to the cabling for the inner and outer cables was about 15% and 30%, respectively. The degradation in the inner layer strand was less severe. Due to a non-optimized strand layout, however, the initial critical current density on virgin strands was already quite low.

Initially, the load-line margin was designed around 10% in both the inner and outer layers. As a result of the large I_c degradation the maximum short sample bore field was reduced to around 11.4 T, with a peak magnetic field of 11.8 T and 9.5 T in

the inner and outer layers, respectively. The load-line margin in the inner and outer layer is therefore similar.

Time constraints in the project did not allow further optimizations of strand layout and cable production, but were considered imperative for a larger scale project. Similar PIT strand-based Rutherford cables made at a later stage after the MSUT, with a more adapted cable design (optimized keystone angle and width/thickness relation) and improved control of cabling settings, did not show such severe degradation.

5.2.3 Mechanical Design

To properly constrain the Lorentz force, a suitable twin-aperture structure was developed with the following design criteria (den Ouden et al. 1992):

- Displacements of the conductor blocks shall be less than 20 μm to minimize field distortions;
- Contact between the yoke halves shall be maintained during excitation;
- The azimuthal compressive stress in the coils shall be preserved after excitation;
- The initial 0.2 mm thickness of the conductor insulation is reduced before the coil heat treatment to 0.14 mm by pressing the wound coil to its final dimensions;
- The equivalent stress shall never exceed the yield stress in any of the used materials;
- The maximum equivalent stress in the coils shall be kept at warm and cold below 150 MPa.

A twin-aperture magnet was analyzed using ANSYS finite element software (ANSYS Inc., Canonsburg, PA). As a starting point, the collar system developed at that time for the LHC dipoles was used. This mechanical system appeared to be insufficient for a 11.5 T dipole magnet. At the location where the two parts of the collar meet, a large stress (Fig. 5.5a) leads to plastic flow of the locking rods and to a loss of pre-stress in the coils. Moreover, the coils are incompletely enclosed by the

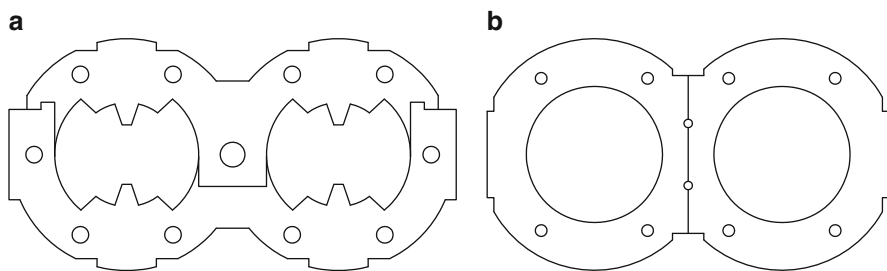


Fig. 5.5 Collar systems for LHC dipole magnets: (a) split collar according to the CERN-LHC reference design; (b) Al-alloy rings. (Modified from den Ouden et al. 1992)

collars in the same region, thus reducing the support area between the coils and collars. To overcome these limitations a ring-shaped shrink-fitted aluminum collar with an increased outer diameter of 110 mm was proposed (den Ouden et al. 1992) (Fig. 5.5b). For the shrink-fit collars Al-alloy 5083 plates with a thickness of 3 mm were chosen for reasons of workability, cryogenic stability, and yield strength.

To achieve pre-stress in the coils at room temperature, stacks of collar plates are heated up to 225 °C and shrink-fitted onto the polyimide ground-insulated coils. Tight tolerances are required for succeeding with the assembly and for achieving a homogenous pre-stress longitudinally along the magnet. The radial space for assembly is limited to about 0.2 mm. In order to better cope with the tight overall tolerances, a cylindrical outer shape of the coil was preferred.

The coils are ring-collared individually and then aligned with central rods to prepare for the yoke assembly (Fig. 5.5b). The yoke plate material is the standard CERN type with a plate thickness of 5 mm. The yoke assembly follows a standard LHC procedure where the two halves are firmly clamped together with an open gap and locked by welding a clamping piece to the yoke halves. During cool-down the gap between the two halves closes and pre-stress in the vertical plane builds up.

A mechanical model of the magnet is shown in Fig. 5.6. A distinct difference from the LHC type of collared coil is the incorporation of separated stainless-steel 316 L pole pieces, which are allowed to slide along the coil pole face. It is important to note that these pole pieces cover both the inner and the outer layers arranged in the

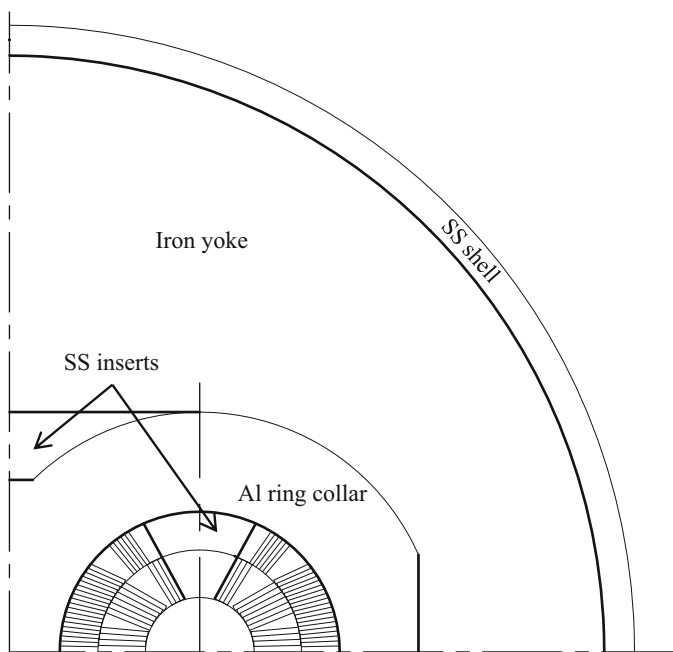


Fig. 5.6 Structural model of the twin-aperture configuration. Bold lines represent the interference layers where friction is included. (Modified from den Ouden et al. 1992)

Table 5.2 Peak equivalent stress in coil and support structures (MPa) for a friction coefficient of $\mu = 0$ (data from den Ouden et al. 1992)

	300 K (I)	300 K (II)	300 K (III)	4.2 K at 0 T	4.2 K at 11.5 T
Coil	63	61	108	116	138
Collar	103	92	124	161	223
Yoke	–	20	192	121	180
Shell	–	–	130	217	219

I = collaring, II = clamping, III = shell shrink-fitting

same plane. The contact between the Al-alloy collars and iron yoke has been optimized such that only the vertical outer planes and the horizontal planes below the triangular yoke insert pieces are in contact. By this approach, the horizontal stiffness of the yoke and shrinking cylinder is transferred efficiently to the Al-alloy collars. Additional pre-compression of the collared coil is realized by shrink-fitting a heated 13.5 mm thick stainless-steel 304 L cylinder around the yoke assembly.

As the sliding planes are metal–metal planes and the uncertainty in the friction coefficient for the metal pairs considered is high, a sensitivity analysis for friction coefficients $\mu = 0, 0.3, 0.4,$ and 0.6 was performed. The equivalent stress in the coil and support structure with a friction of $\mu = 0$ is presented in Table 5.2.

The results show negative effects on the structural dynamics for realistic friction coefficients μ between 0.3 and 0.6. The yoke halves lose contact during excitation, and the inner layer loses contact with the pole insert. The shear stress between the layers increases to unacceptable values (larger than 35 MPa). A reduction of the friction coefficient using Teflon or phosphor-bronze sheets covered with molybdenum-sulfide (MoS₂) powder was therefore considered to impose small friction coefficients even under cryogenic conditions in the order of $\mu = 0.1$ (Tobler 1979; Lizon 1990).

The highest von Mises stress in the coils occur in the mid-plane at the innermost radius. On average, the E modulus for the winding pack was assumed to be in the order of 20 GPa, a value derived from measurements performed on impregnated stacks of PIT-Nb₃Sn-based ECN-SULTAN cable. These measurements showed E moduli in the range 16–21 GPa. A sensitivity analysis revealed that for E moduli below 15 GPa the pre-stress buildup would become insufficient. Moreover, plastic deformation of the copper matrix, which has a yield strength of about 35 MPa after the heat treatment, can be expected. Plastic deformation would also yield to a further and possibly unacceptable reduction of pre-stress in the winding pack. Therefore, work-hardening of the impregnated coils, by pressing them to their final dimensions, before assembly of the Al-alloy ring-collars was seen as a mandatory step during assembly. More details on the twin-aperture mechanical design are presented in den Ouden et al. (1992). The overall cross-section of the coil structure in the straight section is shown in Fig. 5.7.

The results of the mechanical analysis of the twin-aperture magnet appeared to be fairly well applicable to the single-aperture configuration (Fig. 5.8). For the single aperture, closure of the gap between the yoke halves appeared not to be a strict requirement anymore, which allowed for a simplified yoke configuration. A

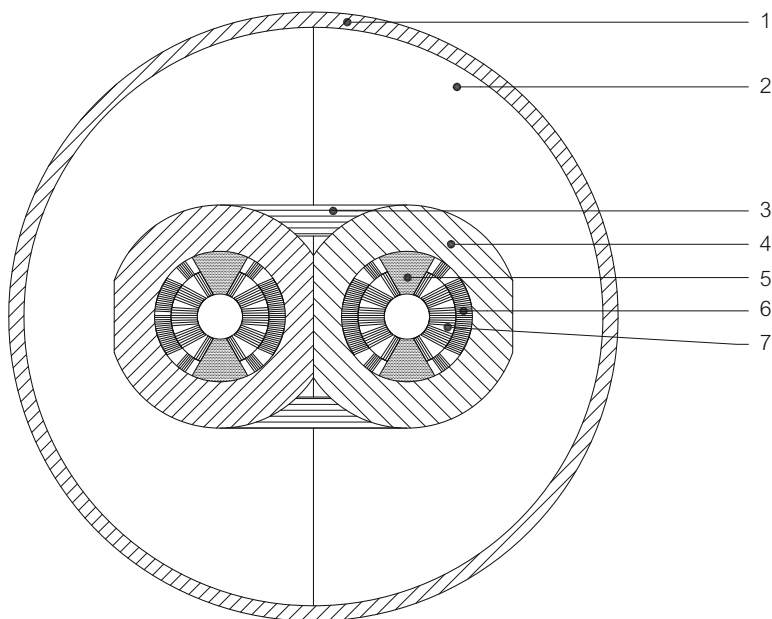
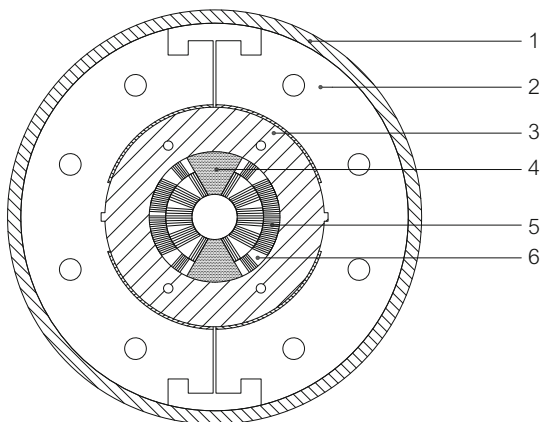


Fig. 5.7 Proposed structural design of the twin-aperture version of the 11.5 T Nb₃Sn LHC dipole magnet (Modified from den Ouden et al. 1992): 1 – outer cylinder; 2 – yoke; 3 – yoke insert; 4 – Al-alloy ring-collars; 5 – pole insert; 6 – conductor block; 7 – copper wedge

Fig. 5.8 Cross-section of the single-aperture magnet showing the coil support system (Modified from den Ouden et al. 1992): 1 – outer cylinder; 2 – yoke; 3 – Al-alloy ring-collars; 4 – pole insert; 5 – windings; 6 – copper wedge



U-shaped aluminum clamp was engineered to hold together the two yoke halves during assembly but it has no structural purpose during cool-down and magnet powering. To prevent excessive stress in the collars due to bending of the yoke halves, the yoke–collar interference was also modified into a circular surface instead of a flat surface. This interference surface is explicitly defined by an arc-shaped zone at the inner radius of the yoke plates around the mid-plane. To simplify assembly and axial pre-stress control, it was decided to not connect the outer stainless-steel

cylinder to the end plates. Instead, eight 20 mm thick tie rods (Fig. 5.8) were used to take up the axial loads and at the same time allowed for a controlled axial preload during assembly.

5.3 Technology Development and Magnet Manufacturing

5.3.1 Cable Degradation Studies

To measure the response of the critical current to transverse pressure applied to an Nb₃Sn Rutherford cable, a dedicated test set-up was developed and installed at the University of Twente (Boschman et al. 1991; ten Kate et al. 1992). In this set-up the wide side of the cable is exposed over a length of 40 mm to transverse mechanical pressures of up to 250 MPa. The critical current at 4.2 K is measured in a background magnetic field of up to 11 T oriented perpendicularly to the wide side of the cable. Currents up to 50 kA are supplied by a superconducting transformer. Impregnated samples of various versions of Nb₃Sn Rutherford cables employing different types of Nb₃Sn strands (bronze, modified jellyroll, internal tin and PIT) were prepared, and their critical current was measured as a function of transverse stress. Some samples of each kind of strand degraded severely and permanently under stress, others showed acceptable behavior.

Figure 5.9 shows the critical current as a function of transverse pressure up to 200 MPa and a field of 11 T for a cable made from ECN PIT strand. The decrease in I_c of $10\% \pm 2\%$ for such a well-impregnated and moderately compacted Nb₃Sn cable is nearly completely reversible, meaning that during re-testing of the cable without applied transverse pressure the cable reached more than 98% of its initial critical current. Based on these and similar results on many other Nb₃Sn cables a general design limit of 150 MPa at cold and warm was formulated, at which only a

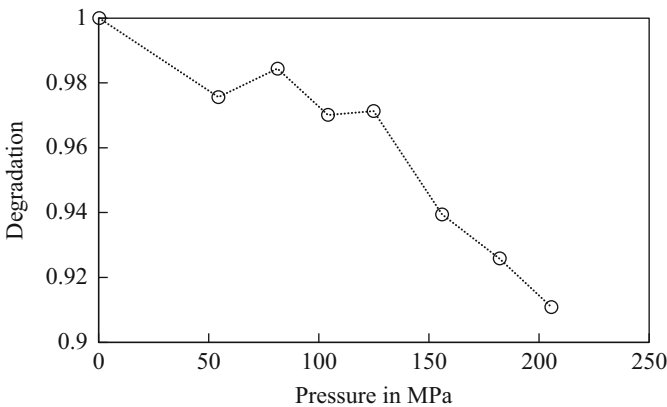


Fig. 5.9 Reduction of critical current density at 11 T vs. applied transverse pressure (voltage criteria 5 $\mu\text{V/m}$). (Modified from ten Kate et al. 1992)

reversible decrease in I_c of less than 10% at 4.4 K is to be expected. It is emphasized, however, that perfect resin impregnation on a strand level of the Rutherford cables in coil windings is essential to guarantee a more-or-less hydrostatic support of the Nb_3Sn layers in the strands of the cables to the imposed stress.

5.3.2 *Mechanical Model*

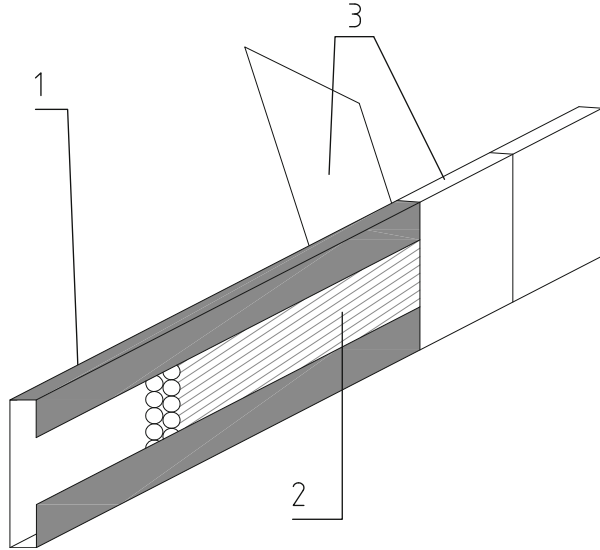
To verify the ANSYS simulation with respect to pre-stress build-up during the collaring process, a 100 mm long mechanical mock-up was built. Because at the time no representative coil blocks were available, the winding layers were replaced by custom-made G10 glass-fiber reinforced cylindrical pieces with a Young's modulus of 25 GPa. The pole inserts were equipped with bridge-type stress gauges. Low friction phosphor-bronze sheets covered with MoS_2 powder were inserted between the pole inserts and the G10 poles. A copper-beryllium tape of 0.4 mm thickness was wound around the coil halves, and phosphor-bronze sheets covered with MoS_2 powder were locked between coil and collars. The aluminum alloy ring-shaped collars were stacked, heated to about 200 °C, and shrink-fitted around the mock-up assembly. The mechanical model confirmed that the required pre-stress could be achieved and that the procedure is suited for at least a 1 m long coil.

5.3.3 *Cable Insulation*

The first trial cable insulation system that could withstand the reaction heat treatment at 675 °C consisted of a direct wrapping of a glass-mica ribbon, applied with 50% overlap. Due to insufficient penetration of epoxy resin through and between the overlapping tape areas, this insulation system resulted in incomplete resin penetration into the voids between the strands, a very low shear strength, and very low thermal conduction between adjacent conductors (den Ouden et al. 1991).

To improve the insulation system, a single sheet of the same glass-mica tape was folded parallel to the cable covering about 70% of its circumference. An S2-glass ribbon was then wrapped manually without overlap around the cable-mica assembly, as shown in Fig. 5.10. The wrapped glass ribbon holds the glass-mica tape in position, improves epoxy penetration into the cable and winding pack, enhances the shear strength between adjacent conductors, and therefore increases the effective thermal conductivity of the insulation layer at 4.4 K by at least a factor of 2. Before applying the Rutherford cable, the S2-glass tape was heat-treated in air at 300 °C to minimize carbon residuals in the coils during the high-temperature reaction heat treatment.

Fig. 5.10 Cable insulation
(Modified from den Ouden
et al. 1991): 1 – folded
glass-mica tape;
2 – Rutherford cable;
3 – S2-glass tape



5.3.4 Coil Wedges and End Spacer Design

To meet the required tolerances, the copper wedges between the winding blocks in coil straight sections have been cut by electrical discharge machine into 140 mm long pieces and afterwards sandblasted to enhance epoxy resin adhesion.

Each conductor block is supported in the coil head by its own end spacer. No further subdivision was foreseen; the spacing between conductors was chosen based on winding tests. The innermost end spacer was made by placing a stainless-steel filler on the mandrel, leaving some space for the block just wound. A 1 mm thick stainless-steel strip was then brazed to a copper wedge and bent a few mm away from the filler into its natural shape. This shape appeared to be a proper inner support for the next turns. The space between the strip and the last turn for the second spacer was filled using a mixture of castable alumina and sand that can easily be removed after the heat treatment. After heat treatment and before resin impregnation, all open spaces were filled tightly with fiberglass. These end spacers were easy to make. They are flexible and form a continuous support path from the straight section into the coil ends, which favors cable mechanical support and prevents damage to the cable insulation and, last but not least, may prevent coil quenching originating from this area.

5.3.5 Coil Winding

Prior to the winding of the Nb₃Sn coils a complete two-layer dummy Nb-Ti pole was wound, heat-treated, stacked, and impregnated. To prevent collapsing of the cables, the winding tension had to be kept within 150–200 N. During coil winding each wound layer was firmly clamped tangentially against the winding poles along the straight parts, in particular close to the ends.

To reduce the effective insulation thickness from 0.20 mm to 0.14 mm the wound coils were inserted in their heat treatment mold and pressed to a precise, pre-defined size with a pressure of about 50 MPa. The coil ends were intentionally left unsupported during all further process steps. Figure 5.11 shows the end region of an outer layer coil after winding (Fig. 5.11a) and after reaction heat treatment (Fig. 5.11b). Figure 5.12 shows a cross-section of the end region of a completely processed Nb-Ti practice coil. The Rutherford cable in the ends shows a remarkable deformation. After some modifications of the end spacer shape this deformation has been suppressed nearly completely during winding of the final Nb₃Sn coils.

Fig. 5.11 Coil fabrication:
(a) coil end after winding;
(b) coil end after reaction
heat treatment

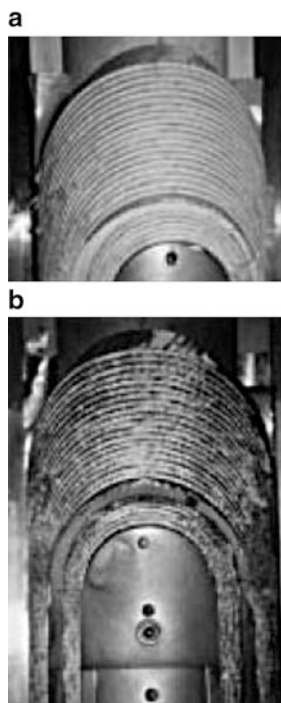
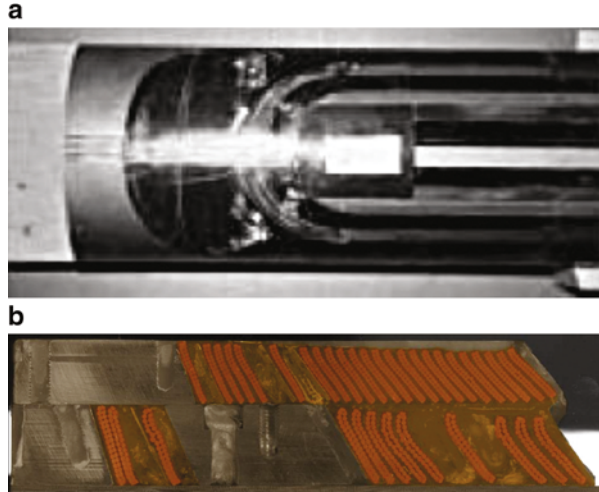


Fig. 5.12 Impregnated Nb-Ti practice coil: (a) top view of the coil end; and (b) lead end longitudinal cross-section



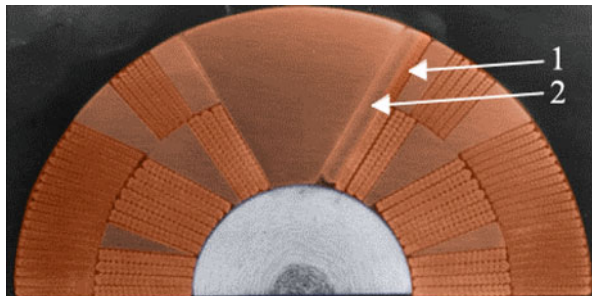
5.3.6 Coil Reaction Heat Treatment

The reaction heat treatment of each single layer placed in its compressed mold took place under vacuum at 675 °C for 14 h. Cable ends were not sealed. During this process, most of the binder material from the glass-mica tape evaporated at around 300 °C and was deposited upon cold surfaces. The remainder did not cause problems with respect to the electrical insulation or binding of epoxy resin. Due to compressing the layer tangentially without axial support, gaps as large as 1 mm between the end spacers and the first conductor of each winding block appeared. As mentioned, these gaps were manually tightly filled with glass-fiber cloth before further processing of the coil layer.

5.3.7 Electrical Connection Between the Coils

To allow for a connection plane between the two coil layers, the outer layer coil was started at the same angle as the pole plane of the inner layer. After separate heat treatment of the coil layers, they were stacked, and a pre-manufactured connection piece consisting of a copper plate was wrapped with Nb₃Sn wires and reacted independently such that it could connect both coil leads. Figure 5.13 shows a cross-section of the splicing area of the dummy Nb-Ti coil. The length of the splice was 450 mm (three twist pitch lengths). The connection piece and coil leads in both layers were thoroughly cleaned with alcohol, brushed with Scotch-Brite[®] pads (3M, Maplewood, MN) and soldered with Ag-Sn solder. To prevent contamination of adjacent windings temporary glass-mica sheets were inserted between the pole and other turns. The resulting resistance at 20 kA ranged from 0.3 nΩ at 0 T to 1.5 nΩ at 10 T.

Fig. 5.13 Dummy coil cross-section: 1 – additional outer layer pole turn (length 450 mm) to match the azimuthal position of the inner layer pole turn; 2 – joint piece jumper, a Cu plate wrapped with heat-treated Nb₃Sn wires



The generated heat of about 0.5 W at nominal operating current and magnetic field was conducted away to the helium bath by an extension of the copper plate, which was installed after impregnation inside the aperture of the final Nb₃Sn coils. This design was acceptable for this test magnet, but would need reconsideration for an accelerator magnet.

5.3.8 Impregnation

Both layers were equipped with G10 end pieces (coil saddles), and temporary Teflon-coated pole inserts. The coil assembly was then placed into an impregnation mold and covered by using the respective parts of the heat treatment mold. Steel foils with a thickness of 50 μm, covered with a non-adhesive layer, were used to ensure release between coils and mold parts.

The resin was Ciba-Geigy MY740 epoxy mixed with HY906 hardener and DY062 accelerator. This resin system was chosen for its demonstrated performance in superconducting magnet systems and for its acceptable pot life of 6 h at 55 °C. The training performance of the resin system was not very well investigated. After vacuum resin impregnation, the final stainless-steel pole inserts were mounted. Two MoS₂ powder-coated phosphor-bronze sliding foils were inserted between the pole inserts and the coils' pole faces to ensure a low friction coefficient at all stages.

5.3.9 Coil Assembly and Collaring

After installation of the instrumentation (see below), the two half-coils were stacked and wrapped with four layers of 0.075 mm thick polyimide foil to ensure sufficient ground insulation. Finally, two 0.20 mm thick, coil-long MoS₂ powder-coated phosphor-bronze sheets were subsequently tightly wrapped around the coils and locked to each other at the mating faces of the second layer by a soft soldered connection.

The precisely aligned and vertically stacked aluminum alloy ring-collar laminations were heated up to 200 °C, which created a 0.20 mm radial gap for the coils, which were quickly inserted vertically into this stack within 10 s. At room temperature, the Al-alloy collars shrunk by 0.08 mm into the coils, providing initial coil pre-stress. After insertion, the heated collars could not be cooled fast enough and heated up the coils to about 90 °C, a temperature at which the solidified epoxy becomes soft and probably yielded. After cool-down, the stress transducers indicated a pre-stress, which amounted to about 30 MPa, 50% of the target value of 60 MPa. Apart from the softened epoxy, the lower-than-expected Young's modulus of the coil may also have added to the lower pre-stress in the coil pack.

5.3.10 Collared Coil Yoking and Skinning

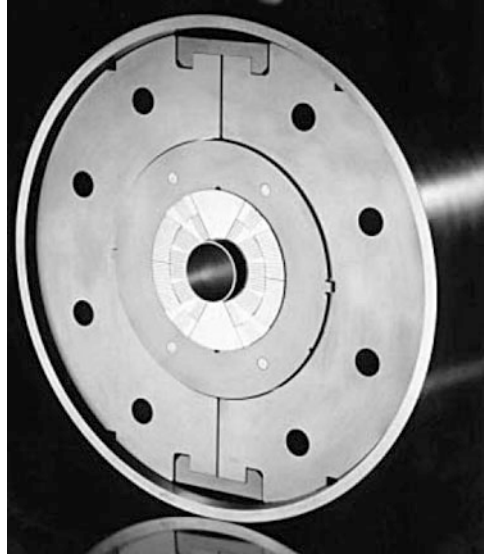
The mounting procedure for the yoke halves and clamping parts was straightforward. Starting in the straight section a few centimeters from the beginning of the coil ends, slightly radially oversized stainless-steel yoke pieces were applied. In the straight section iron blocks were applied. This approach effectively lowered the maximum magnetic field in the coil ends. The magnetic field maximum in both layers is located in the straight section. The yoke was also enclosed by two MoS₂ covered sliding phosphor-bronze foils.

The heated but undersized stainless-steel outer cylinder around the yoke-collared coil assembly should result in a 40 MPa increase of the coil's tangential pre-stress. Despite this increase in pressure, the shrinking process appeared straightforward and fairly easy to control. After axial insertion of eight 20 mm diameter tie rods through the holes in the yoke, 50 mm thick end plates were mounted. The rods were tensioned to supply about 10 MPa axial pre-compression through the end plates to the coil layers alone. For ease of assembly, these end plates were deliberately not welded to the outer cylinder. Figure 5.14 shows a cross-section of the assembled coil and support structure.

5.3.11 Instrumentation and Quench Heaters

Before stacking the two two-layer poles together, each inner layer block was equipped at the inner side with miniature germanium resistors (diameter 1.6 mm, length 5 mm), which were used as thermometers. The sensitivity is of a few kΩ/K with a resistance of typically 10 kΩ at 4.2 K and a relatively low magnetoresistance of less than 3% at 8 T (Zarubin et al. 1990). The thermometers were inserted in small copper tubes that were soft soldered onto a single strand of a particular coil turn. The tubes and about 10 mm of the sensor wires were thermally insulated by 1 mm thick polyimide domes that were glued onto the tubes and sealed by epoxy resin.

Fig. 5.14 Cross-section of the assembled coil and support structure



Strain gauges ($100\ \Omega$) were mounted on similarly mounted copper tubes at the inner layer, which served as a spot heater for the study of normal zone propagation.

Furthermore, many voltage taps were soldered to individual coil turns by locally removing the insulation after resin impregnation.

For measurement of the tangential pre-stress at the poles, bridge-type strain gauges were integrated in the pole inserts.

At the bore side of the inner layer, four meander-shaped, polyimide insulated quench stainless-steel heaters were glued to the coil, covering all windings. These heaters, however, appeared to be ineffective for quench protection. No inter-layer or outer layer quench heaters were foreseen.

5.4 Test Results

The magnet was tested in 1995 for 3 weeks at the model magnet test facility at CERN at a temperature of 4.4 K. After a rather long thermal cycle, the magnet was then retested in 1997. Since the quench heaters appeared ineffective for protection, at least 50% of the stored energy was extracted during quenches. A detailed summary of the test results is presented in den Ouden et al. (1997a, b).

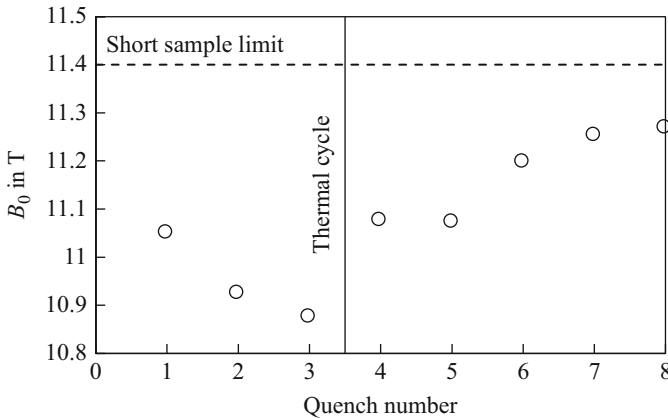


Fig. 5.15 Magnet training history. (Modified from den Ouden et al. 1997b)

5.4.1 Magnet Training

After first cool-down, the magnet was ramped without a quench to 15 kA and, after a flat top of a few minutes, the ramp was continued with a ramp rate of 2 A/s until quench. The first high-field quench occurred at a current of 18.7 kA, corresponding to a record central dipole field of 11.03 T.

A second run immediately after the first quench resulted in a quench current of 18.5 kA (10.92 T), about 1.5% lower than the first quench. After a 3 week measurement program, a third (and for this run, final) high current ramp resulted in a quench at 18.4 kA (10.86 T). A thermal cycle was then performed, and re-testing 2 years later resulted in a first quench at 18.8 kA at a bore field of 11.07 T. The magnet trained in the four subsequent quenches to a maximum current of 19.1 kA and a field of 11.27 T. Note that in these tests the ramp rate was slightly increased to 5 A/s. Figure 5.15 shows the magnet training history.

For quench localization, a static pick-up coil set was used (Bottura 1995). All quenches of the first test occurred in the outer layer of the same pole in the splice region, where the field current margin is the lowest. At many ramps during the entire test campaign, large voltage spikes were observed at low currents, indicating large-scale flux jumps, although without causing the magnet to quench.

5.4.2 Magnetic Measurements

The MSUT transfer function (TF) vs. the magnet current is shown in Fig. 5.16. Due to the relatively small iron yoke outer diameter, its saturation starts at low currents, and at 12 kA the TF reduction reaches ~13%. At currents above 8 kA the curve flattens, indicating that the yoke is practically fully saturated.

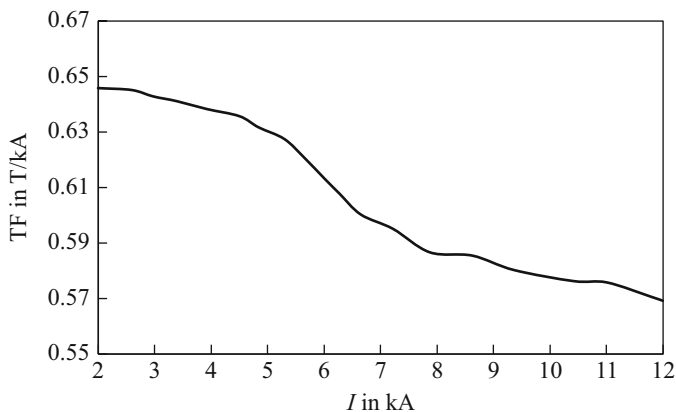


Fig. 5.16 Transfer function vs. magnet current measured at a ramp rate of 10 A/s in the straight part of the magnet. (Modified from Bottura 1995)

Table 5.3 Normalized multipoles $b_n = B_n/B_1$ and $a_n = A_n/B_1$ at constant magnetic field, measured in the straight part (10^{-4}) at a reference radius of 10 mm

B_0 , (T)	b_2	a_2	b_3	a_3	b_4	a_4	b_5	a_5
0.4	-8.4	-21.0	55.8	-4.2	0.7	-3.3	-2.1	-1.6
9.0	-3.3	0.9	-4.4	-1.0	-0.3	-0.6	-0.3	-0.3

In view of possible use in the LHC, the field quality of this magnet was measured at a low field of 0.4 T, which is slightly below the LHC injection field of 0.54 T, at a high field of 9 T, and during magnetic field ramping. At low magnetic fields the most significant field errors originate from persistent filament magnetization currents, whereas at high fields they are affected by iron saturation. During ramping of the magnetic field, inter-strand coupling currents (ISCCs) and boundary induced coupling currents (BICCs) cause additional field errors. Note that the two Rutherford cables used in MSUT did not have a stainless-steel core, which already at that time was considered necessary to limit magnetization effects and magnet ramp losses.

The results of static field measurements are summarized in Table 5.3. The large normal b_2 and skew a_2 quadrupole components may be caused by a combination of small misalignments of the coils and asymmetry in the permanent vertical gap between the yoke halves. The positive sign for b_3 at 0.4 T indicates that at this field the coil re-magnetization process is not complete (see Fig. 5.17).

Figure 5.17 presents the normal sextupole b_3 vs. the magnet bore field measured with a current ramp rate of 10 A/s (corresponding to ~ 6 mT/s) in the magnet straight part and a reset current of around 250 A. The persistent current effect at low fields below ~ 4 T is the main contributor to b_3 due to the $40 \mu\text{m}$ effective filament diameter and the high J_c in superconducting filaments at low magnetic field. The b_3 reaches its minimum of -15 units at a bore field of ~ 1.25 T. Note that these values are affected by the reset current. The asymmetry of the two branches at high fields is due to iron saturation. The iron saturation effect in b_3 , however, is much smaller than in the TF.

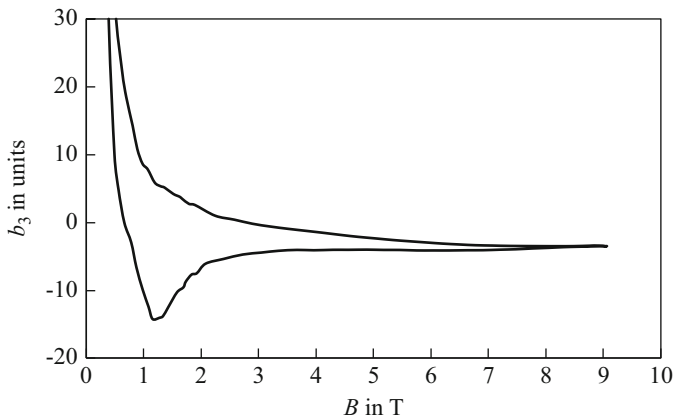


Fig. 5.17 The sextupole component b_3 over the magnetic field measured with a ramp rate of 10 A/s in the straight part of the magnet at $R_{\text{ref}} = 10$ mm. (Modified from Bottura 1995)

5.4.3 Losses During Ramping

The integrated hysteresis and coupling losses during magnetic field cycles were measured electrically (Siemko et al. 1995). Figure 5.18 shows the integrated total hysteresis (extrapolated for a theoretical ramp rate of 0 A/s) and coupling losses during field cycles between 1.9 and 3.8 T for both poles. From these measurements, an average value for the resistance between crossing strands $R_c = 1.2 \mu\Omega$ and a time constant of $\tau = 11$ s were calculated. During the heat treatment at 675 °C the uncoated Cu surfaces of the strands are probably sintered, which results in this very low R_c . The systematic difference between the different coils points to a small difference in the average R_c (R_{c1} , R_{c2}).

5.4.4 Ramp Rate Sensitivity

Figure 5.19 shows the quench currents at different ramp rates for linear ramps from 0 A until quench. Two different types of coil quenching were identified based on the analysis of the voltage tap measurements. At moderate ramp rates ($dI/dt \leq 75$ A/s), the normal and boundary-induced coupling currents are responsible for the relatively fast decrease of the quench current with increasing ramp rate (quench type 1). AC loss measurements show a very low average inter-strand resistance of $1.2 \mu\Omega$. Together with the large cable width, the long cable twist pitch, and the number of strands, this results in relatively high coupling currents. At fast ramp rates ($dI/dt \geq 75$ A/s), large voltage differences between the two poles were observed just before the quench occurred (60–120 mV, duration 10–15 ms). Analysis of the quench location showed that such quenches (labeled quench type 2), exclusively

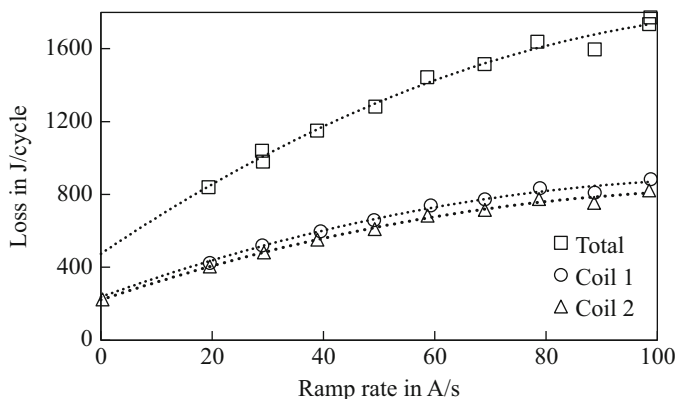


Fig. 5.18 Measured integrated hysteresis and coupling losses as a function of current ramp rate during a 1.9–3.8–1.9 T cycle for both poles separately and the total loss

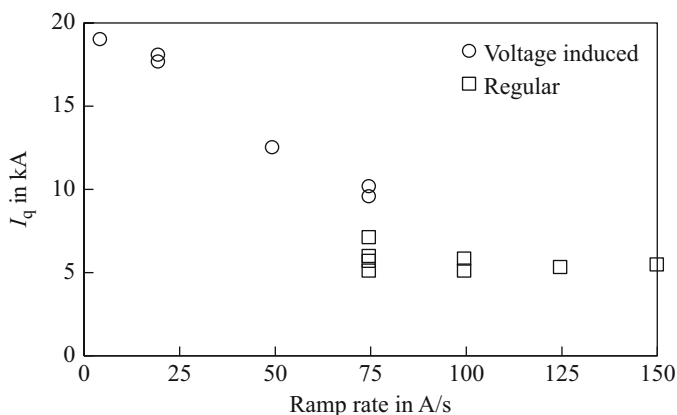


Fig. 5.19 Quench current as a function of ramp rate (circles: regular type 1; squares: type 2). Each ramp started from 0 T. (Modified from den Ouden et al. 1997b)

originated in or near the splice region of one particular pole. For ramp rates at $dI/dt \approx 75$ A/s both types of quenches occur.

5.4.5 Temperature Development

During all magnetic field sweeps, the temperature development in the inner layer conductor blocks was measured with the temperature sensors. Figure 5.20 shows the temperature in the mid-plane block during ramps from 0 to 5 T with ramp rates of 10 to 60 A/s. Due to the high magnetization loss a large temperature rise at low fields

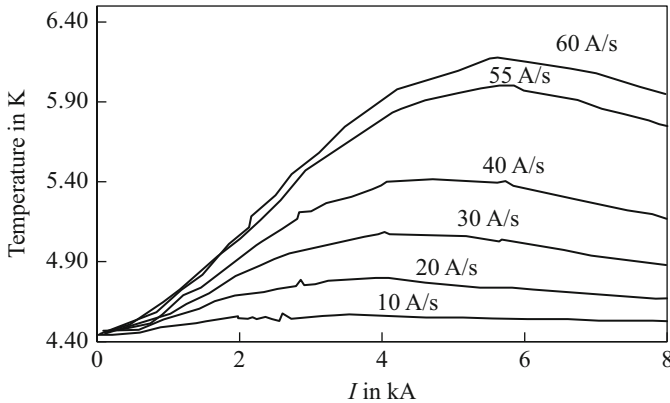


Fig. 5.20 Measured temperature development in the mid-plane block during a field sweep from 0–5 T at different ramp rates

occurs. At the end of the ramp, the magnetization contribution is negligible and only the coupling loss determines the local temperature. Given the measured value for R_c , the calculated temperature increase and the location of the maximum agree very well with the measurements. These unique in situ experiments show the reliability of the thermometer layout and are a valuable tool in the study of the thermal behavior and stability at cable level.

5.4.6 Quench Propagation Velocity

Strain gauges installed on a single strand of the inner layer pole turn were used as a spot heater. Quenches induced in this location spread under quasi-adiabatic condition and cause a quench of the entire pole turn cable within a few milliseconds. The quench propagation in the inner layer was recorded with both the voltage taps and the thermometers. Results were found to be consistent. The difference in the measured voltage between the poles was used to estimate the turn-to-turn propagation, which was cross-checked with measurements from the voltage turn signals. Figure 5.21 shows the turn-to-turn propagation times (Fig. 5.21a) and the normal zone propagation velocity (Fig. 5.21b), obtained from the series of experiments described above.

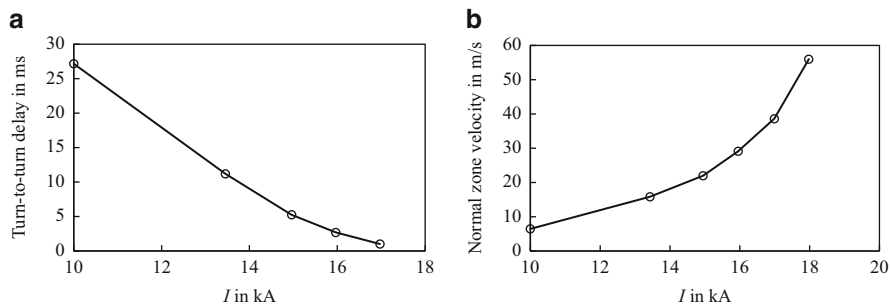


Fig. 5.21 (a) Turn-to-turn propagation times for the pole blocks; and (b) normal zone propagation velocity. (Modified from den Ouden et al. 1997b)

5.5 Conclusion

In the framework of the LHC research and development program, twin- and single-aperture dipole magnets were designed based on PIT-Nb₃Sn high current density conductors. In 1995 the dipole magnet was successfully tested, reaching a record bore magnetic field of 11.03 T at 4.4 K. This result was achieved on first cool-down and first quench of the magnet, which is, even today, a remarkable result given the usual long training curves experienced in other similar Nb₃Sn dipole magnets. After only seven training quenches the magnet reached a bore field of 11.27 T, around 99% on the load line of the cable taking into account the cable degradation during cabling.

The project addressed successfully the development of high current density and high-performing PIT-type Nb₃Sn composite wires, their application in wide cables, and glass-mica cable insulation. The program also brought forward the first systematic electromagnetic optimization of the cross-section of dipole magnets; the application of mechanical structure based on a shrink-fit Al-alloy round collars; coil end spacer designs without discontinuities between the coil ends and the straight section; the introduction of sliding planes based on phosphor-bronze sheets covered with MoS₂ powder; and an innovative layer-to-layer joint using a superconducting shunt. Finally, the uttermost relevance of being able to fill gaps in the winding pack after the reaction heat treatment with glass-fiber fillers to prevent crack formation and propagation cannot be underestimated, as shown by the very good training behavior of this magnet.

The manufacturing and testing experience also revealed a number of challenges, which confirmed that Nb₃Sn accelerator magnet technology remained tedious, costly, and not yet ready for industrialization at that time, as required for series construction of LHC dipoles. The main points, which were seen as being critical towards better performance, were the significant and hard-to-predict conductor performance degradation during cabling as well as the magnetization and coupling current effects. For accelerator operation, the magnet had too large magnetization

and coupling currents with a negative impact on both static and dynamic field quality. The use of a resistive stainless-steel core in the cable helps drastically to reduce the magnetization effects and is nowadays routinely applied. At that time, the filament diameter was seen as a major issue, and development towards smaller filaments while maintaining a high critical current density was considered necessary to reduce drastically the magnetization effects. Dedicated correction schemes are now studied to mitigate the superconductor magnetization effects.

The stress in the magnet did not yield any reduction of performance, which confirmed the mechanical reliability of the PIT conductor and motivated the continuation of the development of this conductor technology in the following decades (den Ouden et al. 2001; Boutboul et al. 2009).

Finally, it is important to realize that one of the primary goals of the MSUT magnet was to achieve 11 T field level. Bearing this in mind, the UT-CERN MSUT program was a great success. It is noted that most of the new ideas (such as wide and stiff high-current cables, continuous end spacers, layer joint jumper, shrink-fit collars etc.) were never all reproduced together in later magnets. It is therefore very hard to correlate without speculation the remarkable MSUT test results—achieving 11 T design field at first cool-down without any training, not yet shown again in later magnets—to one or more of the newly applied current technical solutions.

References

- Boschman H, Verweij AP, Wessel S et al (1991) The effect of transverse loads up to 300 MPa on the critical currents of Nb₃Sn cables. *IEEE Trans Magn* 27(2):1831–1834. <https://doi.org/10.1109/20.133551>
- Bottura L (1995) Results of magnetic measurements on the MSUT (Nb₃Sn) model dipole. Technical Note, AT-MA Note 95–104, July, CERN, Geneva
- Boutboul T, Oberli L, den Ouden A et al (2009) Heat treatment optimization studies on PIT Nb₃Sn strand for the NED project. *IEEE Trans Appl Supercond* 19(3):2564–2567. <https://doi.org/10.1109/tasc.2009.2019017>
- Claudet G, Aymar R (1990) Tore Supra and He II cooling of large high field magnets. In: Fast RW (ed) *Advances in cryogenic engineering*, vol 35. Springer, Boston, pp 55–67
- Den Ouden A, ten Kate HHJ, Wessel S et al (1991) Thermal conduction in fully impregnated Nb₃Sn windings for LHC type of dipoles. *Adv Cryo Eng* 38B:635–642. <https://research.utwente.nl/en/publications/thermal-conduction-in-fully-impregnated-nb3sn-windings-for-lhc-type>
- Den Ouden A, ten Kate HHJ, ter Avest D et al (1992) Analysis of the mechanical behaviour of an 11.5 T Nb₃Sn LHC dipole magnet according to the ring collar concept. *IEEE Trans Magn* 28(1):331–334. <https://doi.org/10.1109/20.119878>
- Den Ouden A, Wessel S, Krooshoop E et al (1994) An experimental 11.5 T Nb₃Sn LHC type of dipole magnet. *IEEE Trans Magn* 30(4):2320–2323. <https://doi.org/10.1109/20.305740>
- Den Ouden A, Wessel S, Krooshoop E et al (1997a) Application of Nb₃Sn superconductors in high-field accelerator magnets. *IEEE Trans Appl Supercond* 7(2):733–738. <https://doi.org/10.1109/77.614608>
- Den Ouden A, ten Kate HHJ, Siemko A et al (1997b) Quench characteristics of the 11 T Nb₃Sn model dipole magnet MSUT. In: Liangzhen L, Guoliao S, Luguang Y (eds) *Proceedings of fifteenth international conference on magnet technology (MT-15)*, 20–24 Oct 1997 Beijing, pp 339–342

- Den Ouden A, Wessel WAJ, Kirby GA et al (2001) Progress in the development of an 88-mm bore 10 T Nb₃Sn dipole magnet. *IEEE Trans Appl Supercond* 11(1):2268–2271. <https://doi.org/10.1109/77.920312>
- Hornsveld EM, Elen JD, van Beijnen CAM et al (1988) Development of ECN-type niobium-tin wire towards smaller filament size. *Adv Cryo Eng* 34:493–498
- Lizon JL (1990) Comparison between various lubricants at cryogenic temperatures in a vacuum. *Adv Cryo Eng (Materials)* 36B:1209–1215
- Perin R (1973) Calculation of magnetic field in a cylindrical geometry produced by sector or layer windings. Internal note CERN: ISR-MA/RP/cb, CERN, Geneva
- Siemko A, Billan J, Gerin G et al (1995) Quench location in the superconducting model magnets of the LHC by means of pick-up coils. *IEEE Trans Appl Supercond* 5(2):1028–1031. <https://doi.org/10.1109/77.402726>
- Ten Kate HHJ, den Ouden A, ter Avest D et al (1991) Development of an experimental 10 T Nb₃Sn dipole magnet for the CERN LHC. *IEEE Trans Magn* 27(2):1996–1999. <https://doi.org/10.1109/20.133597>
- Ten Kate HHJ, Weijers H, Wessel S et al (1992) The reduction of the critical current in Nb₃Sn cables under transverse forces. *IEEE Trans Magn* 28(1):715–718. <https://doi.org/10.1109/20.119979>
- Ter Avest D, ten Kate HHJ, van de Klundert LJM et al (1991) Optimizing the conductor dimensions for a 10–13 T superconducting dipole magnet. *IEEE Trans Appl Supercond* 27(2):2000–2003. <https://doi.org/10.1109/20.133598>
- Tobler RL (1979) A review of antifricition materials and design for cryogenic environments. *Adv Cryo Eng (Materials)* 26:66–77. https://doi.org/10.1007/978-1-4613-9859-2_5
- Zarubin LI, Nemish IY, Szmyrka-Grzebyk A et al (1990) Germanium resistance thermometers with low magnetoresistance. *Cryogenics* 30(6):533–537. [https://doi.org/10.1016/0011-2275\(90\)90055-h](https://doi.org/10.1016/0011-2275(90)90055-h)

Open Access This chapter is licensed under the terms of the Creative Commons Attribution 4.0 International License (<http://creativecommons.org/licenses/by/4.0/>), which permits use, sharing, adaptation, distribution and reproduction in any medium or format, as long as you give appropriate credit to the original author(s) and the source, provide a link to the Creative Commons licence and indicate if changes were made.

The images or other third party material in this chapter are included in the chapter's Creative Commons licence, unless indicated otherwise in a credit line to the material. If material is not included in the chapter's Creative Commons licence and your intended use is not permitted by statutory regulation or exceeds the permitted use, you will need to obtain permission directly from the copyright holder.

